



# Crystal plasticity modeling of transformation plasticity and adiabatic heating effects of metastable austenitic stainless steels

Matti Lindroos<sup>a,\*</sup>, Matti Isakov<sup>b</sup>, Anssi Laukkanen<sup>a</sup>

<sup>a</sup> Integrated Computational Materials Engineering, VTT, Espoo, Finland

<sup>b</sup> Tampere University, Materials Science and Environmental Engineering, Tampere, Finland

## ARTICLE INFO

### Keywords:

Crystal plasticity  
Transformation induced plasticity  
Microstructure  
Adiabatic heating

## ABSTRACT

Strain induced phase transformation in metastable 301LN stainless steel generates a heterogeneous multiphase microstructure with a capability to achieve excellent strain hardening. The microstructural deformation mechanisms, prior deformation history and their dependency on strain rate and temperature determine much of the desired dynamically evolving strength of the material. To analyze microscale deformation of the material and obtain suitable computational tools to aid material development, this work formulates a crystal plasticity model involving a phase transformation mechanism together with dislocation slip in parent austenite and child martensite. The model is used to investigate microstructural deformation with computational polycrystalline aggregates. In this context, material's strain hardening and phase transformation characteristics are analyzed in a range of quasi-static and dynamic strain rates. Adiabatic heating effects are accounted for in the model framework to elucidate the role of grain level heating under the assumption of fully adiabatic conditions. The model's temperature dependency is analyzed. The modeling results show good agreement with experimental findings.

## 1. Introduction

Metastable austenitic steels have a great potential as engineering materials because of their good strain hardening capability combined with excellent ductility. In 301LN stainless steel, inherent strain induced martensitic transformation outstandingly enhances strain hardening of the material (Talonen et al., 2005; Isakov et al., 2016; Järvenpää et al., 2017), making it a typical conceptual material in the wide scope of modern Transformation Induced Plasticity Steels (TRIP) used in the industry (Liu et al., 2018). The mechanical properties of 301 LN stainless steel are affected by various factors, such as composition, grain size, strain rate, and temperature. Besides the well-known unique hardening behavior with early minimum followed by pronounced peak hardening rate, which takes place at low strain rates, e.g., Talonen et al. (2005) observed decreasing phase transformation rate with increasing strain rate. They also noted that the resulting shifting of the work-hardening peak to higher strains improves the overall ductility of the material (Talonen et al., 2005). It is also well established that the phase transformation is strongly sensitive to temperature, i.e., the phase transformation tendency can change from almost full transformation at low temperatures to negligible transformation at higher temperatures over a temperature interval of around 100 K (Olson and Cohen, 1975).

This relationship to temperature appears also at high strain rates because of adiabatic heat generation during plastic deformation. It is clear that the effects of external loading conditions on the overall performance depend much on the microstructure and its evolution. Huang et al. (2012) analyzed the effect of grain refinement to material's yield strength and thermomechanical processing conditions to provide a view on the optimal grain size. Järvenpää et al. (2018) utilized austenite reversion method after cold rolling to analyze grain size effect on tensile properties and evaluate reversed austenite stability. The 301LN material experiences a notable initial strengthening with decreasing grain size at partial expense of overall ductility. In general, refinement of grain size can stabilize austenite, while non-uniformly sized grain structure together with precipitates further enhances heterogeneous transformation process, altering material's strain hardening response (Järvenpää et al., 2017). Grain size has also been observed to cause a change in the dominant fracture mechanism from shear band deviated to grain boundary type dominated fracture, when a transition from coarse grained microstructure to fine or ultra-fine grain sizes is realized (Järvenpää et al., 2014). Larour et al. (2013) and Isakov et al. (2016) further found that strain and strain rate history have a significant role in the overall strength of the material because of the pre-existing changes in the initial microstructure introduced by

\* Corresponding author.

E-mail address: [matti.lindroos@vtt.fi](mailto:matti.lindroos@vtt.fi) (M. Lindroos).

<https://doi.org/10.1016/j.ijssolstr.2021.111322>

Received 5 January 2021; Received in revised form 28 September 2021; Accepted 21 October 2021

Available online 12 November 2021

This is an open access article under the CC BY license (<http://creativecommons.org/licenses/by/4.0/>).

different loading paths. Furthermore, recent study (Vázquez-Fernández et al., 2019a) has shown that strain rate and adiabatic heating have separate roles in phase transformation kinetics. Given all these perspectives linked inextricably to microstructure, a clear need exists to formulate a micromechanical model involving transformation plasticity and ultimately methodology to address microscale damage, to be able to make use of the 301LN material's potential, further the design of respective stainless steels and to understand the observed phenomena.

Various modeling efforts have been made to capture and explain the essential nature of transformation plasticity from phenomenology to engineering purposes. Macroscale models often enrich continuum plasticity models with phase transformation capabilities that affect the hardening behavior of the material and generate volumetric dilation. Engineering purposed approaches are driven by the need to understand and differentiate between detrimental or material enhancing strain localization, for example influencing effective stress-strain state in terms of formability of TRIP steels (Tomita and Iwamoto, 1995; Papatriantafillou et al., 2006; Hallberg et al., 2007). Isakov et al. (2016) placed effort on introducing stronger strain rate and temperature dependencies to extend model's predictive capabilities for complex loading conditions. Micromechanically based approaches are commonly used to quantify the essential deformation and hardening mechanisms in more detail (Fischer et al., 2000; Delannay et al., 2008; Choi et al., 2009; Fischlschweiger et al., 2012). Full crystal plasticity models with or without explicit microstructures provide further insight to grain scale phenomena (Roters et al., 2010). The general ingredients include distinguishing transformation systems in crystalline frame and introducing micromechanical driving force for the transformation, as proposed by Turteltaub and Suiker (2005, 2006b) and Turteltaub and Suiker (2006a). Tjahjanto et al. (2006b, 2008) and Tjahjanto et al. (2006a) further added functionalities to the same crystal plasticity model to concurrently address dislocation plasticity and transformation plasticity and to utilize the model for predictions in thermo-mechanical processing. Yadegari et al. (2012) used similar model for the investigation of thermo-mechanical deformation in multi-phase steels.

Srivastava et al. (2015) verified 3D microstructure based modeling results with micropillar experiments to develop phase-specific plasticity responses in multiphase steels. Alley and Neu (2013) used a crystal plasticity model to investigate hardening effects generated by retained austenite. Lee et al. (2010) successfully correlated strain rate and adiabatic heating effects to transformation rate at quasi-static strain rates in their modeling approach. Sun et al. (2016) enveloped  $\gamma \rightarrow \alpha'$  and  $\gamma \rightarrow \epsilon$  transformation plasticity together with deformation twinning to be able to predict extra-ordinary hardening behavior in twinning induced plasticity (TWIP) steels experiencing also phase transformations. To reduce computational cost of full field 3D models, fast Fourier transformation (FFT) models have been used (Otsuka et al., 2018). In general, micromechanical models used in conjunction with full field 3D microstructural models can be seen advantageous when developing new multiphase steels solutions. This also serves as one of the main motivations for the present work. Among others, Park et al. (2019) focused on developing a multiscale modeling approach to parametrize and utilize crystal plasticity framework, involving phase transformation, to address the deformation and hardening behavior of 3rd generation advanced high strength steels. The observed extremely high strengths and ductility induced by  $\gamma \rightarrow \alpha'$  phase transformation in a multiphase microstructure make the transformation plasticity as an attractive choice in steel development to date (Sohn et al., 2017).

Present work focuses on formulating and utilizing a crystal plasticity framework with martensitic transformation to address special hardening capability of 301LN stainless steel at a wide range of strain rates. Full field microstructural models are considered valuable in the investigation of intra-granular and inter-granular phenomena including characteristic microstructural deformation, phase transformation, and grain level adiabatic heating. As for the main features of the model, a dislocation density based model is formulated for austenite phase with

multiple hardening interactions, while dislocation slip in newly formed martensite is modeled in a phenomenological frame to allow for plastic deformation in the transformed phase. Phase transformation  $\gamma \rightarrow \alpha'$  is driven by mechanical and thermal contributions, including a strain rate dependency, which is not a widely studied aspect within the scope of the respective crystal plasticity models. The model behavior is validated with strain rate dependent experimental data extending from quasi-static up to dynamic strain rates. The concept of strain rate history is also studied to evaluate the model's capability to take prior microstructure evolution into account. Strain rate jump tests, generating a sudden change in loading rate, are selected to provide experimental basis for the strain rate history effects. The role of adiabatic heating is analyzed to provide information on microstructure scale heating with respect to plastic work and latent heat. Polycrystalline microstructural aggregates are investigated with the formulated finite element (FE) numerical model to visualize and extract microstructure scale phenomena, such as the characteristics of phase transformation provided by the model.

The novel features of current work related to the complex deformation, hardening and phase transformation kinetics of austenitic steels can be summarized as:

- We evaluate effectiveness of a crystal plasticity model with mean field phase transformation character on capturing grain scale strain hardening, strain/strain rate-history effects, and the feasibility of conceptual separation of strain rate and thermal effect in phase transformation kinetics to elucidate experimental observations.
- Grain scale heating and local temperatures are simulated in fully adiabatic conditions, estimating the maximum heating effect. Temperature dependency of the model is viewed against physical aspects of thermally and mechanistically driven phase transformation to address the question related to thermal conversion of plastic work and latent heat release from the phase transformation and their effect on local temperature rise.

## 2. Material and methods

### 2.1. Material

The investigated material is EN 1.4318-2B (301LN) stainless steel, manufactured to 2 mm thin sheets. An experimental program was performed and is presented in detail in Ref. Isakov et al. (2016) to determine material's mechanical behavior under tension. The tests included quasi-static tests with servohydraulic machine and high strain rate tests with Tensile Split Hopkinson Bar (TSHB). This work utilizes the data from these tests to cover a range of three strain rates,  $2 \cdot 10^{-4} \text{ s}^{-1}$ ,  $10^0 \text{ s}^{-1}$ , and  $10^3 \text{ s}^{-1}$ . These strain rates represent low strain rate conditions with minimal adiabatic heating, moderate strain rate with almost fully adiabatic conditions, and a dynamic strain rate with fully adiabatic conditions, respectively. The fitness of the model is then evaluated on these conditions. In addition, mixed mode tests were performed by deforming the material first with a low strain rate of  $2 \cdot 10^{-4} \text{ s}^{-1}$  and then continuing with  $10^0 \text{ s}^{-1}$  to inflict a so called strain rate jump experiment/condition. The objective of this test and corresponding simulation is to further verify material's strain rate and phase transformation sensitivity as well as examine model's capability to introduce strain rate history effects (prior deformation). Fig. 1 shows the material's as-received microstructure prior to any mechanical loading. Low amount of annealing twins exist in the microstructure, which are not explicitly accounted for in the simulations. Of a note is that the simulation results presented throughout the paper utilize synthetic microstructures. One-to-one direct comparison of the experimental and simulated microstructures was not attempted except for a brief trial presented in the Appendix, since specific microstructural characterization data of undeformed/deformed zones in the experimental tensile samples is not available. Nominal composition of the material is listed in Table 1.

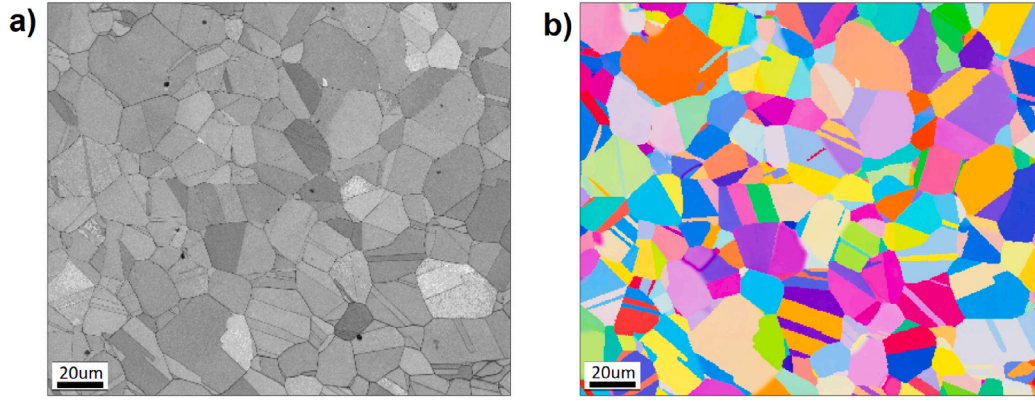


Fig. 1. SEM images of 301LN stainless steel, (a) band contrast, (b) orientation map.

Table 1

Nominal chemical composition of the studied 301LN steel (in wt.-%)

C	Si	Mn	Cr	Ni	N	Fe
0.022	0.38	1.18	17.4	6.7	0.151	bal.

## 2.2. Crystal plasticity model

The following presents the used single crystal model. The model is implemented in the finite element software *Z-set* (Besson and Foerch, 1998). Total deformation gradient is multiplicatively decomposed into elastic, plastic and transformation contributions in the single crystal model. This approach aims to capture the average behavior of the martensitic transformation. The idealized separation does not mean that plasticity by dislocation slip and transformation plasticity would necessarily take place in this particular order. The choice of the order is based on the decomposition of the deformation gradient. Thermodynamical treatment of this multiplicatively constructed model is provided in various studies (Turteltaub and Suiker, 2005, 2006b,a; Tjahjanto et al., 2006a) and Yadegari et al. (2012). The same thermodynamical framework is used as a foundation for the new model features suggested in the present work. Dislocation density based slip model for plasticity in austenite phase follows the main principles of the model proposed by Wong et al. (2016) with novel modifications presented in the following. Furthermore, a rate-dependent model for martensitic transformation is proposed in order to capture strain rate dependency witnessed in the material (Isakov et al., 2016; Vázquez-Fernández et al., 2019a). The deformation gradient is given by:

$$\underline{F} = \underline{F}^e \cdot \underline{F}^p \cdot \underline{F}^{tr} \quad (1)$$

where the effective transformation gradient  $\underline{F}^{tr}$  is constructed as the sum of all available transformation systems and their transformation gradients. The model accounts for 24 Kurdjumov–Sachs type martensitic transformation systems and transformation is considered as volume fraction based mean field model. The volume fraction of each variant is tracked as a contribution to total martensite fraction. The state of the material point can therefore be partially parent austenite and partially various transformation variants. It is clear that the finite element discretization does not aim or suffice to capture the actual spatial scale and the lath martensite formed exactly during the growth process, when presented at the polycrystal level. The transformation part of the deformation gradient is given:

$$\underline{F}^{tr} = \underline{I} + \sum_{\alpha=1}^{N^{\alpha}} f^{\alpha} b^{\alpha} \otimes d^{\alpha} \quad (2)$$

where  $\underline{I}$  is an identity tensor,  $f^{\alpha}$  volume fraction of martensite in variant  $\alpha$ ,  $b^{\alpha}$  is the shape strain vector at the habit plane of martensitic

variant  $\alpha$ , and  $d^{\alpha}$  is the plane normal vector. Only non-reversible transformation is considered in the present context.

Plasticity velocity gradient accounts for dislocation slip taking place in parent austenite and dislocation slip in the formed martensite phase:

$$\underline{L}^p = (1 - \sum_{\alpha=1}^{N^{\alpha}} f^{\alpha}) \sum_{s=1}^{N^s} \dot{\gamma}^s \cdot \underline{N}^s + \sum_{\alpha=1}^{N^{\alpha}} f^{\alpha} \sum_{m=1}^{N^m} \dot{\gamma}^m \cdot \underline{N}^m \quad (3)$$

where  $\dot{\gamma}^s$  is the slip rate in austenite,  $\underline{N}^s$  is the orientation tensor of a slip system  $s$  in austenite,  $\dot{\gamma}^m$  is the slip rate in martensite and  $\underline{N}^m$  is the orientation tensor of a slip system  $m$  in martensite,

To compute mean stress in the material points involving two-phase structure, the volume averaged elastic stiffness  $\underline{A}^{eff}$  is computed with a rule of mixture for the material points as:

$$\underline{A}^{eff} = \frac{1}{\det(\underline{F}^{tr})} ((1 - \sum_{\alpha=1}^{N^{\alpha}} f^{\alpha}) \underline{A}^A + \sum_{\alpha=1}^{N^{\alpha}} f^{\alpha} (1 + \delta^{\alpha}) \underline{A}^M) \quad (4)$$

where  $\underline{A}^A$  and  $\underline{A}^M$  are the elastic stiffness of austenite and martensite phases, respectively. The volumetric change related to transformation is described with  $\delta^{\alpha} = b^{\alpha} \cdot d^{\alpha}$ . This change is equal for each transformation system.

### 2.2.1. Dislocation slip in austenite

The slip rate in austenite is defined by a viscoplastic flow rule:

$$\dot{\gamma}^s = \left\langle \frac{|\tau^s| - (\tau_{pass}^s)}{K^s} \right\rangle^{n^s} \text{sign}(\tau^s) \quad (5)$$

where  $\tau^s$  is the resolved shear stress,  $\tau_{pass}^s$  is the isotropic hardening term providing resistance against flow,  $K^s$  and  $n^s$  describe viscosity.

Slip resistance in terms of passing strength is given by:

$$\tau_{pass}^s = \mu_A b^s \sqrt{\sum_{j=1}^{N^s} H_{sj} (\rho_e^s + \rho_d^s)} \quad (6)$$

where  $\mu$  is the shear modulus of austenite phase,  $b^s$  is the length of Burgers vector for slip,  $\rho_e^s$  is the density of edge dislocations and  $\rho_d^s$  dipole dislocation density according to the model proposed by Wong et al. (2016). The interaction matrix  $H_{sj}$  describes the magnitude of each interaction type and the coefficients can be estimated by using dislocation dynamics based simulations (Devincere et al., 2006).

Evolution of edge dislocation density is controlled by storage and annihilation terms:

$$\dot{\rho}_e^s = \left( \frac{1}{b^s \Lambda^s} - \frac{2d_{mgl}^s}{b^s} \rho_e^s - \frac{2d^s}{b^s} \rho_e^s \right) |\dot{\gamma}^s| \quad (7)$$

where  $\Lambda^s$  is the mean free path for slip. The dislocation dipole density evolves according to:

$$\dot{\rho}_d^s = \frac{2d_{mgl}^s}{b^s} \rho_d^s |\dot{\gamma}^s| - \frac{2d^s}{b^s} \rho_d^s |\dot{\gamma}^s| - \frac{4v_{climb}}{(d_{mgl} - d^s)} \rho_d^s \quad (8)$$

where two distances control annihilation process. Distance  $d_{mgl}^s$  is the maximum slip plane distance that two dislocations can have to form a dipole and  $d^s$  is the annihilation distance for two edge dislocations. The two distances are given by:

$$d_{mgl}^s = \frac{3Gb^s}{16\pi|\tau^s|} \quad (9)$$

$$d^s = C_{anni}b^s \quad (10)$$

where  $C_{anni}$  is the annihilation fitting parameter. Climb velocity is presented as:

$$v_{climb} = \frac{3\mu D_0 \Omega}{2\pi k_B T} \frac{1}{d_{mgl}^s - d^s} \exp\left(\frac{-Q_c}{k_B T}\right) \quad (11)$$

where  $D_0$  is self-diffusion coefficient for FCC iron,  $\Omega$  and  $Q_c$  are the activation volume and the activation energy for climb, respectively.

Mean free path (MFP) affects the evolution of dislocation density and thus the slip resistance. In this view, the material's strain hardening is affected by dislocation–dislocation interactions and the formation of new martensite phase, and by collective grain size effects. All of these contributions are placed in the evolution of effective mean free path along with grain size  $d$ :

$$\frac{1}{\Lambda^s} = \frac{1}{d} + \frac{1}{\Lambda_{slip}^s} + \frac{1}{\Lambda_{sliptrans}^s} \quad (12)$$

The contribution from dislocation interactions reads:

$$\frac{1}{\Lambda_{slip}^s} = \frac{1}{i_{slip}} \left( \sum_{s=1}^{N^s} H_{sr} \sqrt{\rho_e^s + \rho_d^s} \right) \quad (13)$$

where  $i_{slip}$  controls the magnitude of hardening. Transformed new phase is expected to generate dislocation storage through the reduction of mean free path by dynamically decreasing the effective grain size and acting as strong barriers for dislocations. The hardening effect is driven by the volume fraction of martensitic phase:

$$\frac{1}{\Lambda_{sliptrans}^s} = \sum_{s=1}^{N^s} H_{sa} f^a \frac{1}{t_a (1 - \sum_{a=1}^{N^a} f^a)} \quad (14)$$

where  $t_a$  is the average lath thickness and essentially a fitting parameter,  $H_{sa}$  is the interaction matrix between slip and transformation systems controlling the hardening intensity in the model.

### 2.2.2. Martensitic transformation

Driving force for the martensitic phase transformation can be written decomposed as (Tjahjanto et al., 2006a):

$$f^i = f^m + f^{th} + f^d + f^s \quad (15)$$

where the contributions are mechanical  $f^m$ , thermal  $f^{th}$ , defect energy  $f^d$ , and surface energy  $f^s$ . The separation of each contribution makes the model physically more tangible and allows to define each contribution multiphysically in the spirit of better retaining a connection to the underlying physical mechanisms. Future efforts could be placed to unravel parametrization of each contribution separately.

The mechanical contribution to the driving force is estimated based on Ref. Tjahjanto et al. (2006a) and given by:

$$f_a^m = J_{tr} \underline{F}^{pT} \cdot \underline{F}^{eT} \cdot \underline{F}^e \cdot \underline{S}^e \cdot \underline{F}^{p-T} \cdot \underline{F}^{tr-T} (b^a \otimes d^a) + \frac{1}{2} (\underline{\Lambda}^A - (1 + \delta_{tr}) \underline{\Lambda}^M) \underline{E} \cdot \underline{E} \quad (16)$$

which involves the dominant stress contribution and an elastic mismatch correction term between austenite and martensite, respectively.  $\underline{E}$  is the Green–Lagrange strain tensor. Thermal part of the driving force is approximated by a single most dominant term in contrast to the extended approach used in Yadegari et al. (2012):

$$f^{th} = \rho_0 \frac{\lambda_T^a}{\theta_T} (\theta - \theta_T) \quad (17)$$

where  $\rho_0$  is the mass density of the material,  $\lambda_T^a$  is latent heat of martensitic transformation,  $\theta_T$  is the transformation temperature, and  $\theta$  is the current temperature.

The remaining two contributions, defect and surface energies are written:

$$f^d = \frac{\omega_A}{2} (\mu_A - (1 + \delta_{tr}) \mu_M) \beta_d^2 \text{ and } f^s = \frac{\chi}{l_0} (2f^a - 1) \quad (18)$$

where  $\omega_A$  is considered as a scaling or a fitting parameter describing defect energy in austenite,  $\chi$  is the interface energy per unit area and  $l_0$  is a length-scale parameter. Shear modulus of austenite and martensite are  $\mu_A$  and  $\mu_M$ , respectively.  $\beta_d$  can be used as representation of microstrain variable to account for elastic distortions generated by dislocations (Tjahjanto et al., 2008). However, its effect in the overall contribution was found negligible and following reasoning is given also for the terms  $f_s$  and  $f_d$ .

In this context, the so called surface energy term is used to describe the stored elastic energy at the newly formed interfaces of austenite and martensite. The twinned martensite platelet thickness can be associated with the austenite grain size. This formulation develops a phenomenological grain size dependency for the surface energy contribution on driving force, i.e., smaller grain sizes makes the transformation energetically more expensive (Turteltaub and Suiker, 2006a). In the view of the simplifications pointed out in Ref. Turteltaub and Suiker (2006a) related to defining surface energy for multiple concurrently active martensite variants, we choose to set this term to zero and compensate its effect directly in the value of critical transformation stress. Similarly, we do not characterize directly the energy stored in elastic lattice distortions accounted by defect energy term (Tjahjanto et al., 2008, 2006a). In spite we acknowledge these effects, and argue this choice justified with the objective of this work to envisage mainly the effects of mechanical stress (strain rate) and thermal contributions (adiabatic heating) on phase transformation and hardening behavior. Furthermore, in the case of utilizing the material parameters related to surface and defect energy in refs Turteltaub and Suiker (2005) and Tjahjanto et al. (2008) for TRIP steels with the present model, their overall contribution was found much lower than direct mechanical and thermal parts with the parameters used hereafter for 301LN steel.

Martensitic transformation is modeled by a kinetic growth rule with a strain rate dependency, as given in Eq. (19). The choice of rate dependent form is reasoned by recent observations (Vázquez-Fernández et al., 2019a) showing that strain rate alone can have a strong role in phase transformation kinetics, while concurrently occurring adiabatic heating has a contributing role. The rate dependent flow rule then separates these two effects in the model.

$$\dot{f}^a = \left\langle \frac{(f_a^m + f^{th}) - f^{cr}}{K^a} \right\rangle^{n^a} \quad (19)$$

Here the two main driving forces promote martensitic transformation, i.e., stress assisted transformation  $f_a^m$  and thermally driven transformation  $f^{th}$ , as discussed above. The rate-dependent form is applied at microscale so that it can reproduce the observation that the phase transformation depends on the apparent strain rate at macroscale (Isakov et al., 2016). The transformation rate is modeled with viscoplastic flow rule, introducing two viscous parameters  $K^a$  and  $n^a$ . From computational perspective, the rate-dependent form does not need unique choice of active system(s) with rate-independent algorithms. However, in turn, it does not exactly provoke a single system dominated flow at the material points, yielding a mean field approach from the model.

Nucleation criterion in the model is fulfilled when the combined driving force exceeds the critical threshold  $f^{cr}$  for the transformation. The threshold value has been estimated for a crystal plasticity model using  $f^{cr} = 549 - 0.994Ms$  [MPa] (Turteltaub and Suiker, 2005). However, uncertainties exist related in defining martensite start temperature as well as the general applicability of various Ms-temperature defining equations for the present metastable material. Due to this reasoning,



the  $f^{cr}$  is determined based on the experimental data, reflecting on the relationship of applied strain and volume fraction of martensite in tensile experiments at various strain rates.

### 2.2.3. Dislocation slip in martensite

Dislocation slip in martensite is considered possible in the model. It is, however, expected that newly formed martensite contains a high dislocation density, which delays the onset of slip up to high shear stress state. The question related to the density and structures of the dislocations in transformed martensite is not addressed here due their complex nature inherently related to the transformation process, and also, this is a future work item necessitating its own dedicated experimental and characterization work. A viscoplastic phenomenological model is thus used for the martensite phase and the slip rate is provided with:

$$\dot{\gamma}^m = \left\langle \frac{|\tau^m| - (R^m)}{K^m} \right\rangle^{n^m} \text{sign}(\tau^m) \quad (20)$$

where  $R^m$  is the slip resistance of a slip system  $m$ ,  $K^m$  and  $n^m$  are viscous parameters. Total of 24 slip systems are used, comprising slip system families 12  $\{110\}\langle 111 \rangle$  and 12  $\{112\}\langle 111 \rangle$ . The slip resistance consists of an initial shear resistance  $\tau_0^m$  and an isotropic hardening part. The initial shear resistance represents the total resistance in transformed state for the martensite phase, including solid solution contribution, dislocation density and contribution of any existing defect structures, which are not in current work treated separately.  $R^m$  is given by:

$$R^m = \tau_0^m + Q_m \sum_{p=1}^{N^p} H_{pm} \{1 - \exp(-b_m v^p)\} \quad (21)$$

where  $Q_m$  controls the magnitude of hardening,  $N^p$  is the number of slip systems (totaling 24 in BCC),  $H_{pm}$  is the interaction matrix between slip systems, and  $b_m$  describes the saturation behavior. Cumulative plastic slip in system  $p$  is defined  $v^p = \int_0^t |\dot{\gamma}^p|$ .

### 2.2.4. Adiabatic heating

The 301LN austenitic steel exhibits notable heat generation already during intermediate strain rates, such as  $1.0 \text{ s}^{-1}$  (Talonen et al., 2005; Isakov et al., 2016). Therefore, adiabatic conditions are assumed for the simulations performed at intermediate  $1.0 \text{ s}^{-1}$  or dynamic strain rate  $1000 \text{ s}^{-1}$ . Two sources of heat generation are distinguished. Main part of the plastic work generated by dislocation slip is converted to heat, and the heat generation from the martensitic transformation by latent heating is included in the model as a second contribution. Thermal strains are neglected in this work, but temperature affects shear modulus of the material as well as the thermal contribution of phase transformation kinetics. Furthermore, the dislocation climb tendency in austenite is affected by temperature, according to Eq. (11). The rate of heat generation from the above mentioned two sources is formulated in Eq. (22).

$$\Delta\theta = \beta_\theta \frac{\sigma_{eqv} (1 - \sum_{\alpha=1}^{N^\alpha} f^\alpha) (\sum_{s=1}^{N^s} |\dot{\gamma}^s| + \sum_{\alpha=1}^{N^\alpha} f^\alpha \sum_{m=1}^{N^m} |\dot{\gamma}^m|)}{\rho_0 C_v} + \frac{\sum_{\alpha=1}^{N^\alpha} \dot{f}^\alpha H^{\gamma \rightarrow \alpha}}{C_v} \quad (22)$$

where  $\beta_\theta$  is the plastic work to heat conversion factor assumed to 0.9,  $\sigma_{eqv}$  is the equivalent stress, and  $C_v$  is the specific heat capacity. It is worth noting that coefficient  $\beta_\theta$  can be chosen to be different for austenite and martensite phases (Zaera et al., 2013).

## 3. Results and discussion

### 3.1. Model deformation behavior and parametrization strategy

The primary strategy for material single crystal model parameter identification involves the use of polycrystalline aggregate, shown

later in Fig. 6. The synthetic polycrystal contains 180 grains that are randomly oriented in the simulations. Kinematic uniform boundary conditions are applied for the computational microstructure and uniaxial tensile loading is imposed. In the following section, we utilize special elements for the 2D finite element mesh, where a 3D material model is projected so called two and half dimensions available in Zset software Z-set package (2013). The out of plane degrees of freedom are fixed out. Appendix provides additional simulations of the material behavior with 3D microstructural aggregates and also compares the response of an EBSD based microstructure extruded to one element thickness.

#### 3.1.1. Parametrization strategy

Table 2 lists the used single crystal model parameters and the parametrization strategy for each deformation mechanism. For dislocation slip in austenite, the relationship between dislocation storage to annihilation was adjusted with  $C_{anni}$  to generate pre-transformation hardening curvature and then to adjust the competition between the transformation plasticity and the dislocation slip in the parent phase. Experiments at different strain rates were further used to verify the parametrization of dislocation–dislocation hardening  $i_{slip}$  and  $C_{anni}$  in addition to the strain rate dependency of the flow through parameter  $n$ . We set the interaction matrix  $H_{sj}$  for dislocation slip as constant, although its values may change with evolving dislocation density (Monnet and Mai, 2019).

Strategy for phase transformation parametrization is summarized as follows. Critical transformation resistance  $f_{cr}$  and related strain rate parameters  $K^\alpha$  and  $n^\alpha$  were adjusted to comply with the experimental evolution of martensite volume fractions, i.e., comparing averaged volume fractions in the polycrystal RVE with experimentally measured macroscopic values. Strain rate dependent martensite volume fraction evolutions allow the definition of strain rate exponent  $n^\alpha$ , while incubation period of martensite growth is controlled with  $K^\alpha$ . The stress–strain curves (hardening) were utilized to define the interaction strength  $H_{sa}$  relating phase transformation induced barriers to the dislocation slip resistance. Initial yield strength for martensite was chosen high to represent lath martensite with high dislocation density. The initial slip resistance  $\tau_0^m$  was defined to introduce sufficient saturation of hardening curves at very high martensite volume fractions, e.g. tension with a strain rate of  $2 \cdot 10^{-4} \text{ s}^{-1}$  (see next section). Strain rate dependency of martensite was also set low in the spirit of Ref. Lindroos et al. (2017). Finally, the strain hardening parameter  $Q_m$  and its saturation  $b_m$  related to martensite were adjusted to cause only minor hardening with fast saturation. We consider that this choice reflects the behavior of untempered martensite with high yield strength and low strain hardening capability in contrast to autotempered martensitic steels (Lindroos et al., 2017). At present, the coefficients of interaction matrix for child martensite are not considered among the most important parameters of the model and we set equal interactions between all systems for simplicity.

The temperature sensitivity of the model is analyzed in Appendix to evaluate the effect of critical transformation stress  $f^{cr}$  and latent heat  $\lambda_T^\alpha$  on strain hardening and susceptibility to phase transformation.

#### 3.1.2. Strain rate dependency and strain hardening

Fig. 2a represents stress–strain response of the model homogenized over the whole aggregate. The curves show good agreement with the experiments at three strain rates. Fig. 2b shows the predicted and measured martensite volume fractions as a function of macroscopic strain. Strong upward curved strain hardening is observed in Fig. 2c for the quasi-static strain rate of  $2 \cdot 10^{-4} \text{ s}^{-1}$  beyond 10% of strain. This hardening response is much attributed to the transformation plasticity and its relation to dislocation slip in austenite and the new martensite phase. In detail, the phase transformation first causes an apparent decrease in the hardening capability due to activation of this additional deformation mechanism. It is quickly inverted to additional overall

**Table 2**  
Single crystal parameters used in the simulations for 301LN stainless steel.

Parameter		
Elastic constants	Austenite	Martensite
$C_{11}$ [MPa]	197 000	236 000
$C_{12}$ [MPa]	134 000	140 000
$C_{44}$ [MPa]	105 000	116 000
Parameterization strategy		
Ref. (Kadkhodapour et al., 2011)		
Austenite		
$K^s$ [MPa.s <sup>1/n</sup> ]	95.0	Set close to $\tau_0^s$ (CRSS)
$n^s$	15.0	Strain rate experiments
$b^s$ [nm]	2.56	Constant
$d$ [ $\mu$ m]	14.0	Average
$i_{slip}$	50.0	Set with exp. data
$C_{anni}$	5.0	Set with exp. data
$D_0$ [m <sup>2</sup> /s]	4.0e <sup>-5</sup>	Ref. Wong et al. (2016)
$Q_c$ [J]	3.0e <sup>-19</sup>	Ref. Wong et al. (2016)
$h_1 - h_6$ ( $H_{rs}$ )	0.122; 0.122; 0.07; 0.625; 0.137; 0.122;	Ref. Monnet and Mai (2019)
$\mu_A$ [GPa]	$-3.0e^{-5}T^2 - 5.6e^{-3}T + 88$	Ref. Monnet and Mai (2019)
$\beta_{th}$	0.9	Set and varied between 0.5–1.0
$c_v$ [J/kg K]	460	Vázquez-Fernandéz et al. (2019b)
$\lambda_T^a$ kJ/kg	20	Constant
Ref. Isakov et al. (2016)		
Transformation $\gamma \rightarrow \alpha'$		
$f^{cr}$ [MPa]	260.0	Set exp. martensite fractions
$K^a$ [MPa.s <sup>1/n</sup> ]	160.0	Set exp. martensite fractions
$n^a$	10.0	Set exp. strain rate dep.
$t_a$ [m]	1e <sup>-7</sup>	Set for lath martensite
$H_{sa}$	0.075	Set exp. hardening
$\theta_T$ [K]	803	Thermo-Calc® Software
Martensite		
$\tau_0^m$ [MPa]	320.0	Set for hardening saturation
$K^m$ [MPa.s <sup>1/n</sup> ]	320.0	Set equal to $\tau_0^m$ (CRSS)
$n^m$	50.0	Set for martensite based on Lindroos et al. (2017)
$b_m$	15.0	Approximated high saturation rate
$Q_m$ [MPa]	20.	Approximated low hardening rate
$h_1 - h_8$ ( $H_{pm}$ )	All 1.0	Set equal for all systems

hardening character during the spreading of phase transformation in the microstructure and a higher number of barriers existing within the grains for dislocation slip in austenite. The effect of strain rate is twofold at the homogenized aggregate level. First, the typical increase in effective yield stress of the material is seen with increasing strain rate. However, the high strain rate imposes a lowered strain hardening capability that is mainly originating from the decreased martensite formation rate and its influence on dislocation slip in austenite. This decrease in strain hardening capability leads to negative apparent strain rate sensitivity at high strains (flow curves at different strain rates intersect), even though the instantaneous strain rate sensitivity stays positive in all cases, as dictated by the viscous flow rule in the model.

Fig. 2d shows the average increase of temperature in the whole microstructure for the two higher strain rate cases. Adiabatic conditions were assumed in the simulations based on the analysis provided in Ref. Talonen et al. (2005), Isakov et al. (2016) and Vázquez-Fernandéz et al. (2019a). The macroscopic temperature increase exceeds 100 K with the use of conversion factor  $\beta = 0.9$ . This averaged temperature value of the whole microstructure originates from the local scale transformation related latent heat and from the dissipation of plastic work to heat in accordance with Eq. (22). The conversion factor for the transformation induced latent heat generation was set to 1.0. Isakov et al. (2016) observed macroscopic temperature rise of about 80–90 K in thermo-couple measurements away from the main localization site of the tensile specimens, which suggests that the model prediction is reasonably realistic. Vázquez-Fernandéz et al. (2019b) recently used in-situ optical deformation and infra-red-radiation based measurements to investigate the local temperature rise. They observed around 70 K increase in temperature after 35% of true plastic strain deformed at the strain rate of  $10^{-1} \text{ s}^{-1}$  which is also in the range that the model predicts for higher strain rates.

Cumulative and instantaneous slip activities are shown in Fig. 2e, f. The onset of strong martensitic transformation reduces FCC slip activity

due to the increase in slip resistance. This is mechanistically related to the decreasing mean free path and decreasing phase volume fraction. The dislocation densities in austenite reach relatively high values in the FCC slip dominated regions, but phase transformation does not necessarily occur progressively in all orientations in spite of the increased local stresses. When the transformation process approaches complete transformation of material points, the local stresses begin to rise rapidly in the new elastic phase. In the absence of BCC slip, the model would over-estimate the hardening curve drastically. Therefore, the activation of BCC slip is adjusted to provide sufficient saturation of hardening in the  $2 \cdot 10^{-4} \text{ s}^{-1}$  strain rate case. The results show that increasing strain rate decreases the BCC slip activity, owing mostly to the lower amount of martensite transformation and lower local stress states in comparison to the low strain rate loading conditions.

The strain rate dependency of the material was also investigated with strain jump experiments. The strain rate jumps were replicated with the simulation model to validate the simulated material behavior under instantaneous change of loading rate. The model parametrization was performed with the above described data from monotonous strain rate tests. That is, the model parameters were not adjusted to fit the jump experiments. Furthermore, the strain rate jump modeling concept allows one to interpret loading history effects taking place in the material. Fig. 3 presents a comparison between experiments and simulations in a strain rate jump test together with the constant strain rate simulations. Most importantly, it is observed that the simulations are able to predict the sudden increase in flow stress as well as the characteristic change in martensite volume fraction evolution, as seen in Fig. 3a, b. The deformation at the lower strain rate is followed by reduced phase transformation and strain hardening rates when the strain rate is increased. The increase in temperature after the strain rate jump is also distinctive, since at the moment of jump the deformation conditions change from nearly isothermal to adiabatic.

Qualitative comparison of martensite volume fractions for the simulated and experimental microstructures is presented in Fig. 4. In this

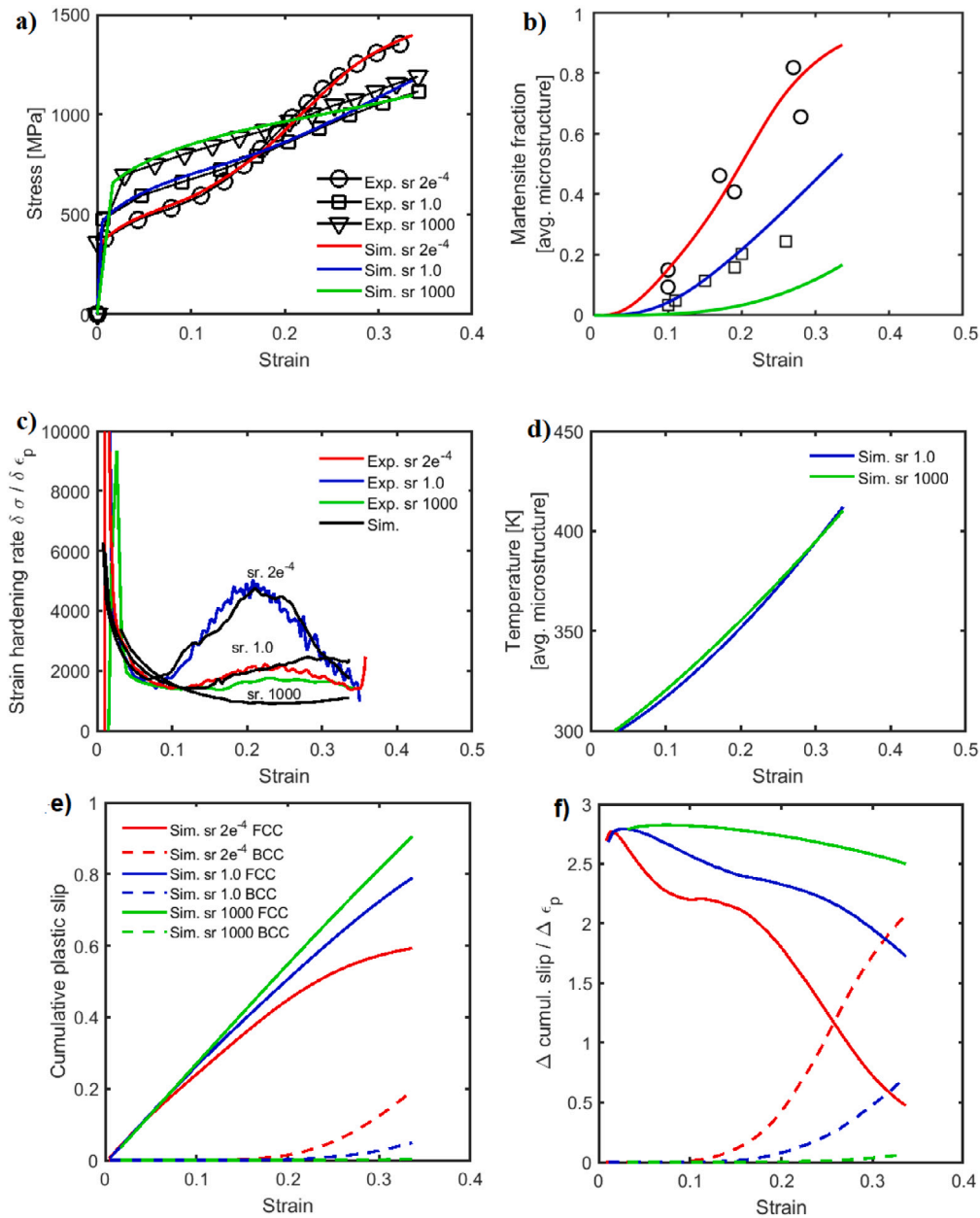


Fig. 2. Simulation and experimental curves for (a) constant strain rates, (b) martensite volume fractions, (c) strain hardening rate, and (d) increase in temperature during deformation produced by adiabatic conditions, (e) cumulative plastic slip for austenite (FCC) and martensite (BCC) crystals, (f) plastic slip rates for austenite and martensite.

Figure the simulation maps show complete transformation with red and partial transformation in gradient coloring. At low strain rate (Fig. 4a) large areas of fully or almost fully transformed grains coexist with partially transformed grains and regions. The martensite in strain rate jump test/simulation in Fig. 4b appears more scattered due to the later stage suppression of the transformation process taking place due to higher strain rate and adiabatic increase in temperature.

### 3.1.3. Grain level heterogeneity

Fig. 5a shows material point level distributions of equivalent plastic strain produced by dislocation slip (sl.) and transformation plasticity (tr.), fraction of transformation material, equivalent stress, and increase in temperature for the strain rate of  $1 \text{ s}^{-1}$ . As seen in Fig. 5b, the transformation process is rather polarized, i.e. majority of the material points are either fully transformed or very mildly transformed. This result indicates that the model provides reasonable resemblance of the incubation period in the transformation process from small scale

nuclei to a rapid formation of the new phase. This characteristic is not necessarily intuitive for mean field finite element models utilizing a volume fraction based transformation model. The stress distributions in Fig. 5c are relatively smooth at the moderate 17% strain. Large amount of grains have not been fully transformed or the slip activity in non-transforming grains has not yet increased dislocation density to very high levels, which both would cause more distinctive heterogeneous hardening and high stresses. It can be speculated based on the simulations that, when the strain is increased, the following hardening scenario is observed. The higher martensite transformation tendency during low strain rate deformation introduces bimodal stress distribution at the end of the tensile test at 34% of strain, which pronounces the heterogeneity effect and the load bearing capacity of the material increases notably. However, this effect is lower in the high strain rate deformation, because of the lower amount of martensite transformation. The local heterogeneities have less prominent effect



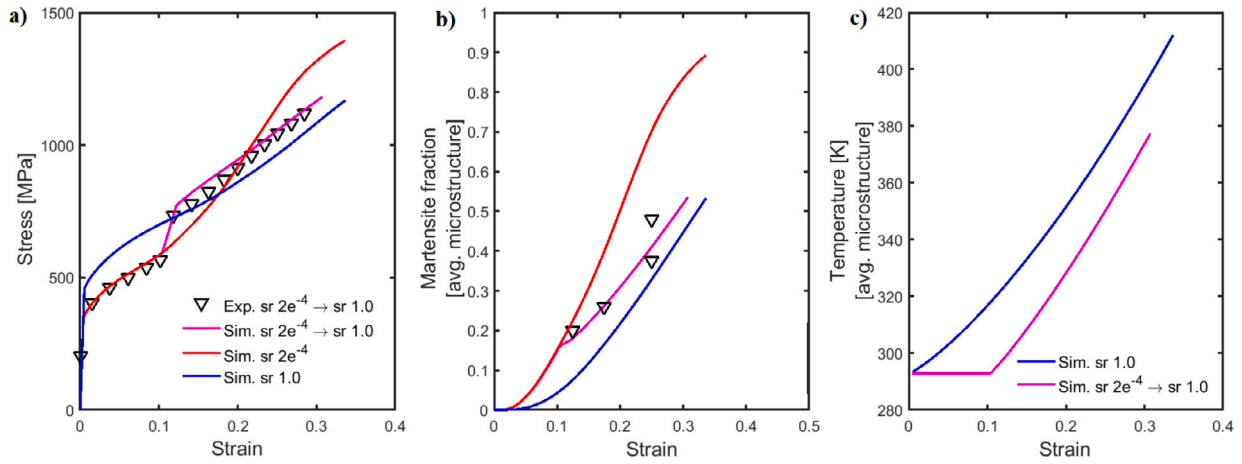


Fig. 3. Simulation and experimental data of strain rate jump test (a) stress-strain curves for two constant strain rates and one with a strain rate jump, (b) evolution of martensite volume fractions, (c) increase in temperature.

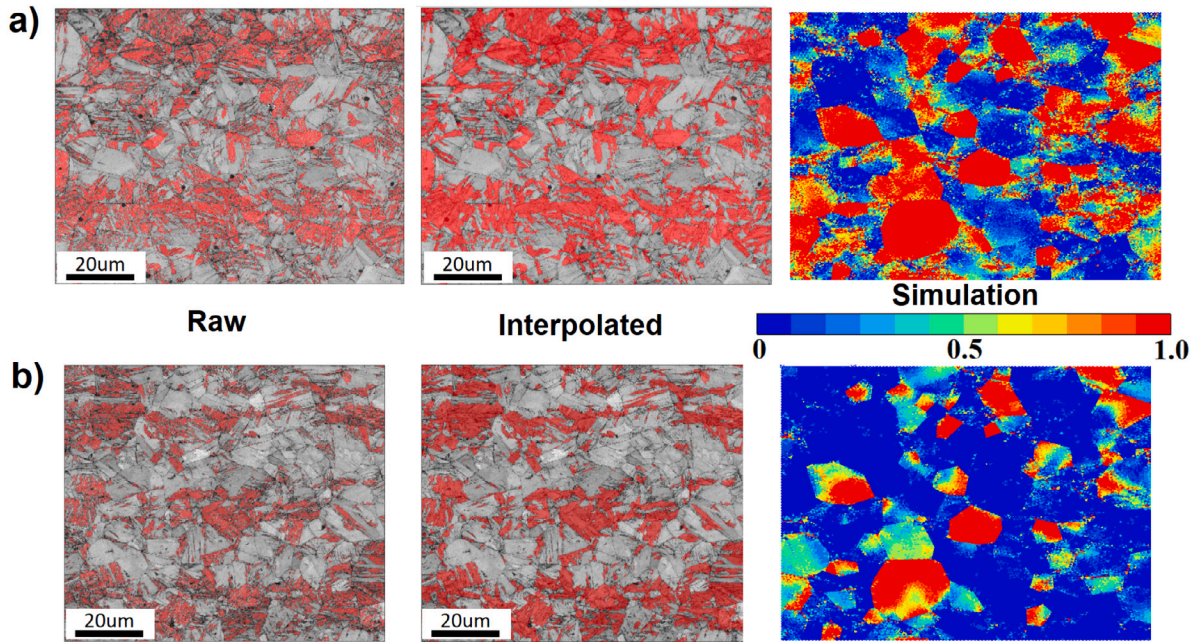


Fig. 4. SEM EBSD band contrast image overlaid with martensite phase and simulated martensite volume fractions, for strain rates (a)  $2 \cdot 10^{-4} \text{ s}^{-1}$  at  $\epsilon_p = 0.19$ , (b) jump test from  $2 \cdot 10^{-4} \text{ s}^{-1}$  to  $1.0 \text{ s}^{-1}$  at  $\epsilon_p = 0.10$ , total  $\epsilon_p = 0.17$ .

on hardening in this case and lower overall strain hardening rate is observed.

Recently, Vázquez-Fernández et al. (2019b) noted that the heat conversion factor  $\beta$  is not constant throughout the deformation history and depends on strain rate for 301 LN. Furthermore, they suggest that typical values of  $\beta = 0.9$ – $0.95$  can represent overestimates. To analyze the effect of  $\beta$  with the model, we revisit the local effects of heat generation. Fig. 5e, f demonstrate the effect of heat conversion factor to microstructure scale heating at the strain rate of  $1 \text{ s}^{-1}$ . To simplify, the value is set constant and independent of previous deformation history. The average temperature increase of the microstructure decreases notably with lower values of  $\beta$ . The shape of the material point level temperature distribution remains essentially the same, but the peak of the distribution is shifted with respect to  $\beta$ . Vázquez-Fernández et al. (2019b) also propose that the change in the measured value of  $\beta$  has significant relation to phase transformation and its latent heat, as AISI 316 steel with no phase transformation showed essentially much less variation in  $\beta$  values throughout the deformation history. This aspect implies that the phase transformation kinetics and the latent heat from

the phase transformation have to be accounted for when the value of  $\beta$  is calibrated with experimental measurements. Further work is therefore needed to accurately simulate the two sources of material heating, i.e., the conversion of plastic work and the latent heat release from the phase transformation. Furthermore, it is not necessarily true that the grain level conditions are fully adiabatic when local hotspots exist, as is assumed in the current model. This assumption thus also calls for future work. However, in any case, it is argued here that grain level heating behavior should be investigated further and accounted for in the simulations of austenitic steel grades featuring complex deformation mechanisms.

Fig. 6 illustrates the final state of the computational microstructure at the true strain of 34%. Stress concentrations appear stronger in the lower strain rate case throughout the microstructure, as was already observed from the density function graphs in Fig. 5. A noteworthy aspect in the simulations is that the extended hardening capability is not only a product of martensite transformation alone. For one, slip localization plays an essential role in the vicinity of non-favorable transformation sites, that are seen in the microstructure. Slip populated



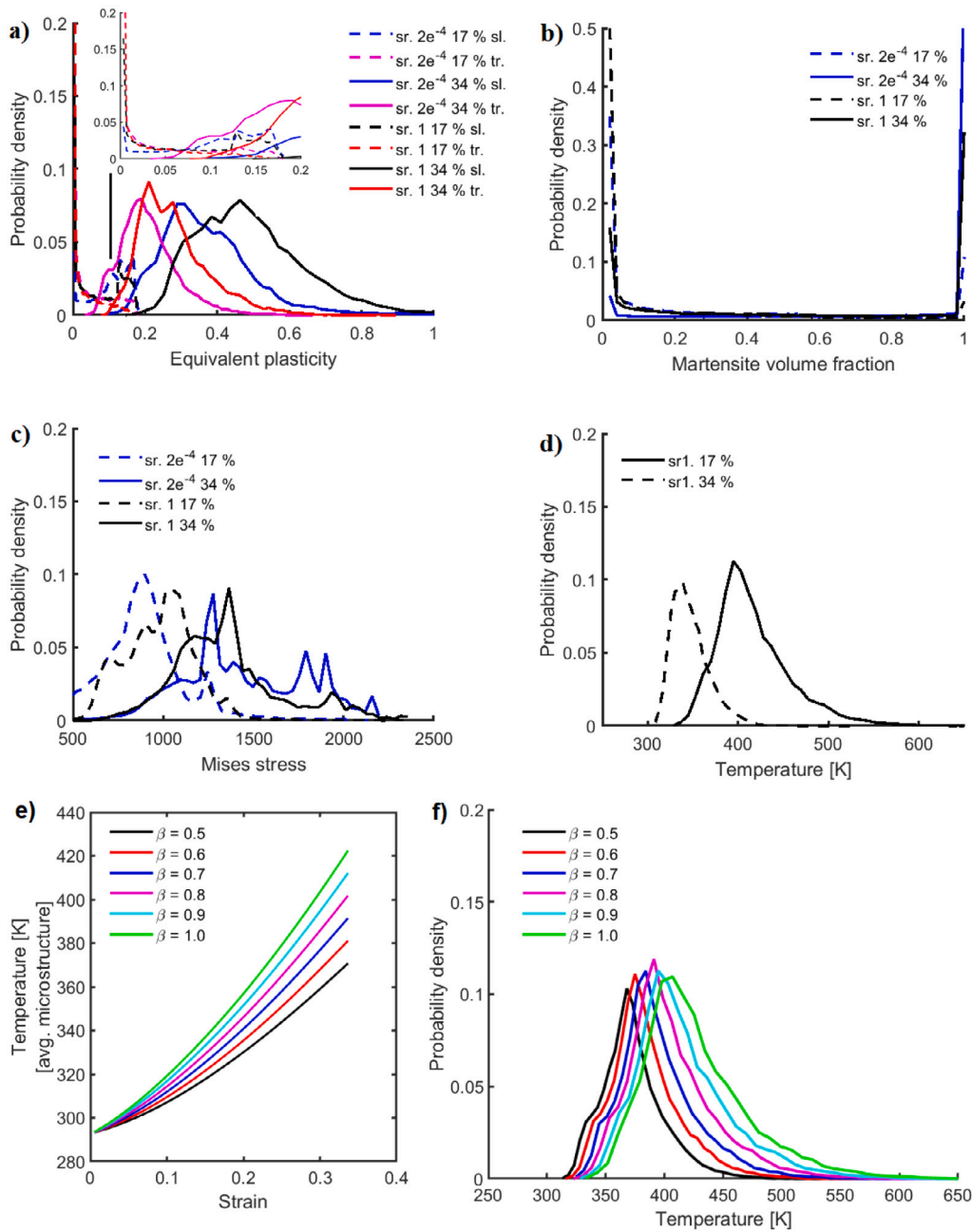


**Fig. 5.** Distributions of (a) plasticity contributions, (b) martensite volume fraction, (c) Mises stress, (d) temperature with  $\beta = 0.9$  for the polycrystalline aggregate at two strain rates. The effect of heat conversion factor  $\beta$  on temperature rise (e) and temperature distribution at the end of tensile test with 34% of strain (f).

zones act as an additional source of hardening when dislocation density (visualized here by the slip strain) is increased substantially. In most cases, however, slip dominated grains behave as crucial sites for accommodating strain that can be understood to have a positive effect on material's ductility via promoting a more uniform state of deformation.

Figs. 5, 6 show that the temperature distribution ( $\beta = 0.9$ ) at the microstructure level is rather heterogeneous. In this case, the primary source for heat generation occurs from the dislocation slip dissipated energy. Latent heat from phase transformation inputs less to the overall range of 20–350 K increase in the local temperature. Most significant local temperature rises, therefore, take place when a slip dominated flow is followed by transformation. These phenomena together increase the local heat generation and the maximum temperature inside the grain. Grain boundary regions appear as zones of special interest. They become susceptible heat concentrated zones in the presence of prior slip driven phase transformation. Soft grains (orientations) can undergo

severe plastic deformation in the hard–soft grain setting, which can be intuitively assumed to promote fracture with grain boundary character due to the influence of slip localization and/or stress concentrations.

#### 4. Conclusions

A crystal plasticity model was formulated to address deformation, hardening and martensitic phase transformation in 301LN stainless steel. Model sensitivity was analyzed in terms of strain rate, strain hardening and temperature. The following summarizes the main observations and conclusions.

- The model using dislocation density based evolution combined with phase transformation and dislocation slip in the transformed phase is able to predict extra-ordinary stress–strain behavior and phase transformation characteristics of 301LN stainless steel with

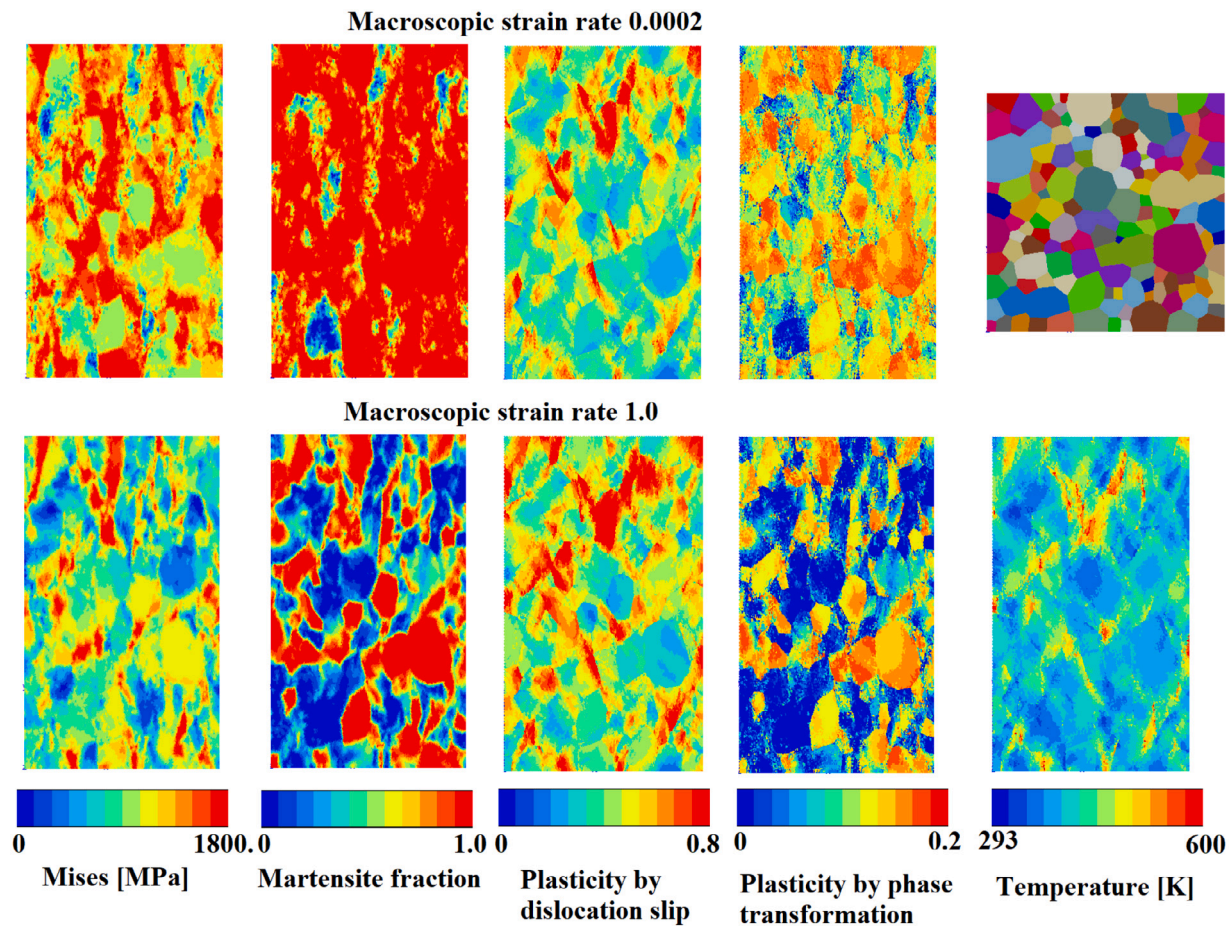


**Fig. 6.** Von Mises stress contours, volume fraction of martensite, cumulative plastic strain by dislocation slip, cumulative transformation induced plastic strain for strain rates  $2 \cdot 10^{-4} \text{ s}^{-1}$  and  $1.0 \text{ s}^{-1}$  including temperature field from adiabatic heating. Axial true tensile plastic strain is 34%.

good accuracy. The material's strain rate dependency is captured from quasi-static strain rates up to dynamic range. Sudden strain rate jump introduces changes in the instantaneous strength, as well as subsequent strain hardening and martensite transformation rates, which is also realistically reproduced by the model. In general, further texture development verification locally and globally could aid to validate model behavior in more detail. The validity of the modeling approach under multiaxial loading is also a noteworthy topic, since in general the martensitic transformation is affected by the stress state.

- Once phase transformation occurs, the model mimics the heterogeneous grain scale rapid phase transformation process which is observed in the experimental post-mortem characterization. The model predicts that single material point is mainly either austenite or martensite, while partially transformed material point represents growing fine scale martensite embryos. Phase transformation kinetics are influenced by strain rate and temperature with both having suppressing effect. The separation of strain rate and temperature sensitivity in the phase transformation kinetic part of the model offers a feasible method to represent recent observations dissociating these phenomena (Vázquez-Fernández et al., 2019a). The model is able to describe temperature dependency of both slip and phase transformation, which allows for a wide range of usability for the model. The prediction capability for relevant flow stress and phase transformation effects, however, depends much on the approximation of temperature dependent parameters of the model.
- When fully adiabatic conditions are assumed at microstructure scale, the experimentally observed macroscopic temperature rise

of from 60 K to around 100 K is explained by a wide range of grain scale temperature rises from 20 K up to 350 K, originating from plastic dissipation to heat and transformation latent heating. Future work is suggested to address the following observations in more detail: (i) the evolution of the heat conversion factor of plastic work to heat has significant influence on the magnitude of microstructure scale temperatures. (ii) The assumption of adiabatic conditions may not hold at low strain rates (e.g.  $0.1\text{--}1.0 \text{ s}^{-1}$ ) or even at  $1000 \text{ s}^{-1}$  at grain scale due to the substantial temperature gradients found in the simulated microstructure.

#### Declaration of competing interest

The authors declare that they have no known competing financial interests or personal relationships that could have appeared to influence the work reported in this paper.

#### Acknowledgments

Prof. Samuel Forest from MINES ParisTech is gratefully acknowledged for valuable discussion and comments on model framework. Prof. Greta Lindwall from KTH Royal Institute of Technology and Dr. Tatu Pinomaa from VTT Research Centre of Finland are acknowledged for the thermodynamical input data with respect to ThermoCalc software. The authors M. Lindroos and A. Laukkanen would like to acknowledge the financial support of Business Finland in the form of a research project ISA VTT Dnro 7980/31/2018.

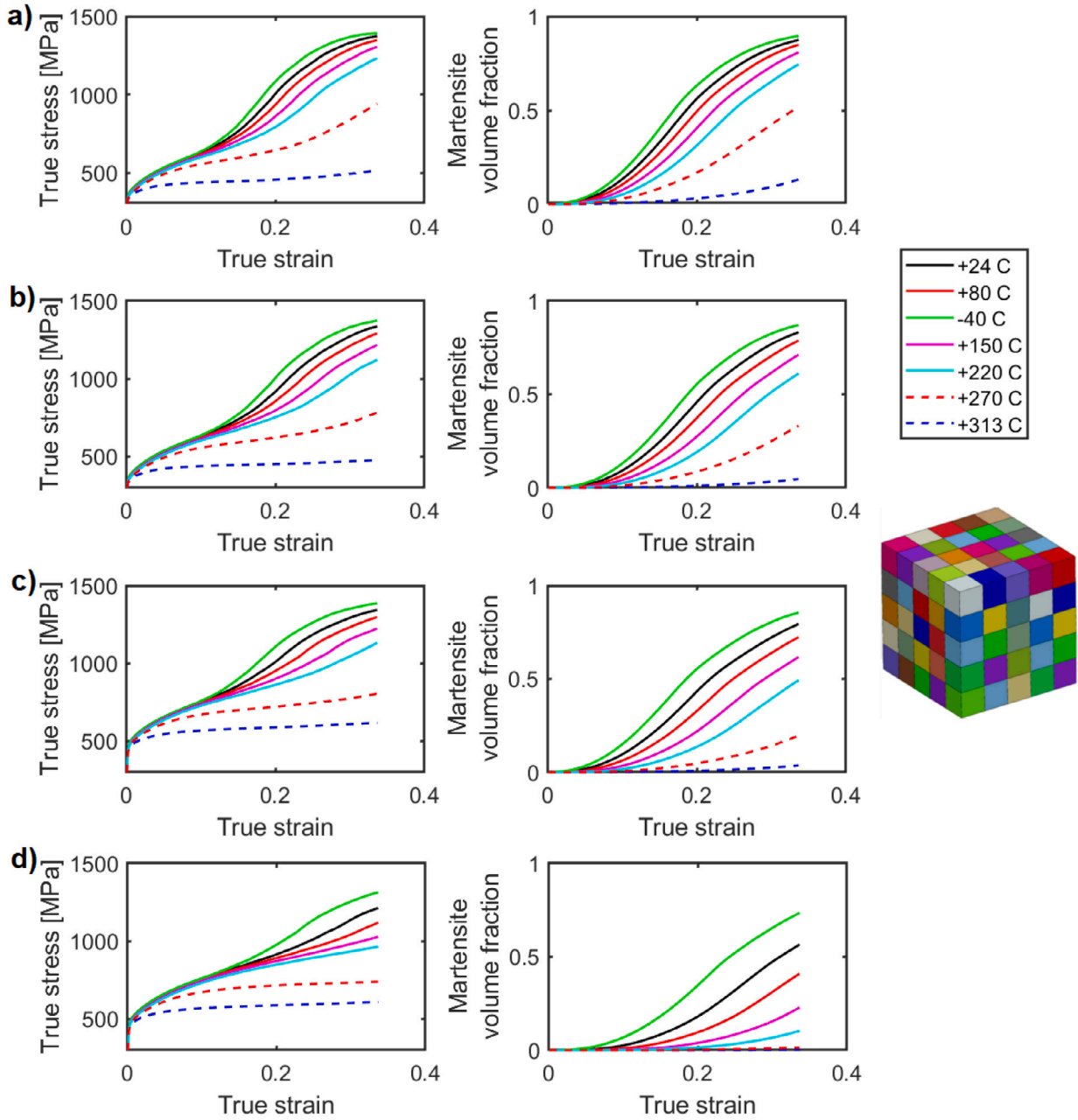


Fig. A.7. Stress–strain curves and martensite volume fractions at different temperatures with (a)  $\theta_T = 803$  K, (b)  $\theta_T = 586$  K, (c)  $\theta_T = M_s = 369$  K (with  $f^{cr} = 265$  MPa and  $\lambda_T^a = 20$  kJ/kg), and (d)  $\theta_T = 369$  K (with  $f^{cr} = 365$  MPa and  $\lambda_T^a = 40$  kJ/kg).

## Appendix. Sensitivity analysis

### A.0.4. Temperature sensitivity

The thermal contribution of driving force for phase transformation is in a crucial role in the process of predicting the temperature dependent transformation kinetics of 301LN steel. To provide an insight to the model's current sensitivity to temperature and its effect on the phase transformation, a parametric study is carried out. We recall that the temperature dependency is introduced in the dislocation model of austenite with the evolution of idealized dipole dislocation density in Eqs. (8) and (11) as well as more directly for the slip resistance through its relation to the temperature dependent shear modulus. In present context, we retain the generalized form for slip in austenite given by Eq. (5) with no direct additional temperature dependency placed on strain rate exponent  $n^s$  or viscous parameter  $K^s$ . As for the

thermal contribution introduced in Eq. (17) ( $f_{th} = \rho_0 \frac{\lambda_T^a}{\theta_T} (\theta - \theta_T)$ ), that is co-driving transformation kinetics with a mechanical contribution, the selection of parameters defining the magnitude of the thermal driving force is not necessarily always straightforward. In particular, the choice of the transformation temperature  $\theta_T$  and the latent heat  $\lambda_T^a$  for the martensite transformation has proportional effect on the magnitude of  $f_{th}$  by the relationship, which then affects the phase transformation rate and its probability. To obtain an approximation for these values, one option is to employ thermodynamical databases to estimate  $\theta_T$  and  $\lambda_T^a$  for a given composition. We utilized the Thermo-Calc (TC) software (and the TFCE9 database) in the current study, which yielded estimations of  $\theta_T = 803$  K and  $M_s \approx 369$  K for the lath martensite.

Given these aspects, a sensitivity analysis is performed with the model. Tensile test simulations were performed with a constant strain rate of  $2 \cdot 10^{-4} \text{ s}^{-1}$  at seven temperatures: 233 (−40 C), 297 K (+24 C), 353 K (+80 C), 423 K (+150 C), 493 K (+220 C), 543 K (+270 C), and



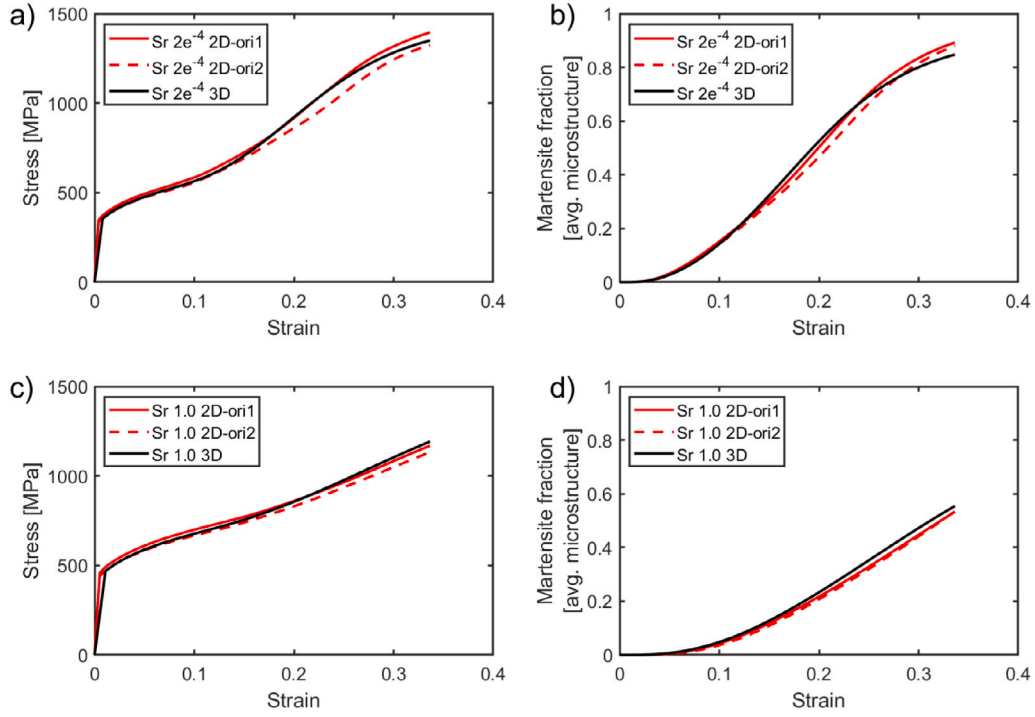


Fig. A.8. Stress-strain curves and evolution of martensite volume fraction of 2D and 3D polycrystal aggregates at strain rates of (a)–(b)  $2e^{-4}$  and (c)–(d)  $1.0 \text{ s}^{-1}$ .

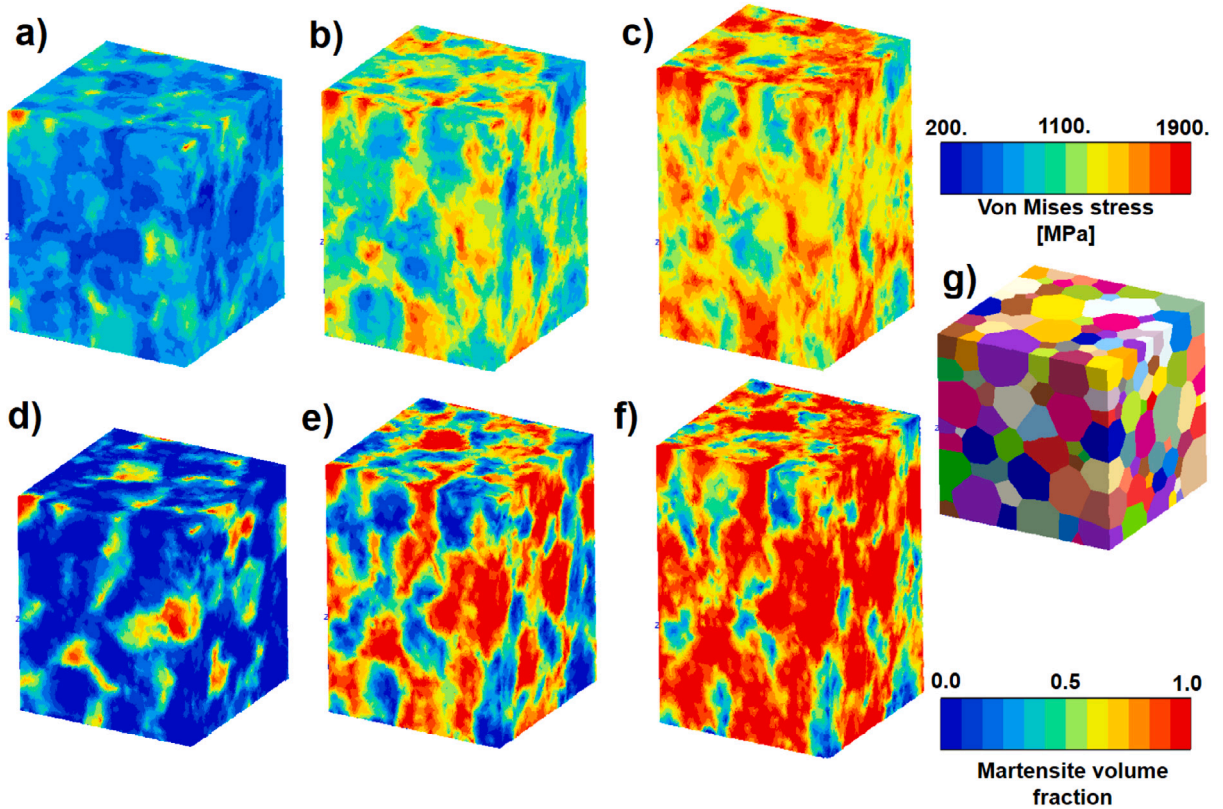


Fig. A.9. Evolution of equivalent stress (a)–(c) and volume fraction of martensite (d)–(f) of 3D polycrystalline aggregate (g). Axial true strains are 10, 20 and 33% deformed at  $2 \cdot 10^{-4} \text{ s}^{-1}$ .

a mean value 586 K (+313 C) between  $\theta_T$  (TC) and  $M_s$  (TC). The value 586 K is also used as an alternative value for  $\theta_T$  to review its effect. Finally we set  $\theta_T = M_s$  in the analysis. Simplified 125 grain microstructural aggregate was used in the simulations with each grain having a

random orientation. One element was assigned for each grain. Fig. A.7 shows stress-strain response and martensite volume fraction evolution with three different  $\theta_T$  and at seven constant temperatures. Latent heat is assumed the same in the sensitivity analysis (Fig. A.7a–c) in spite of

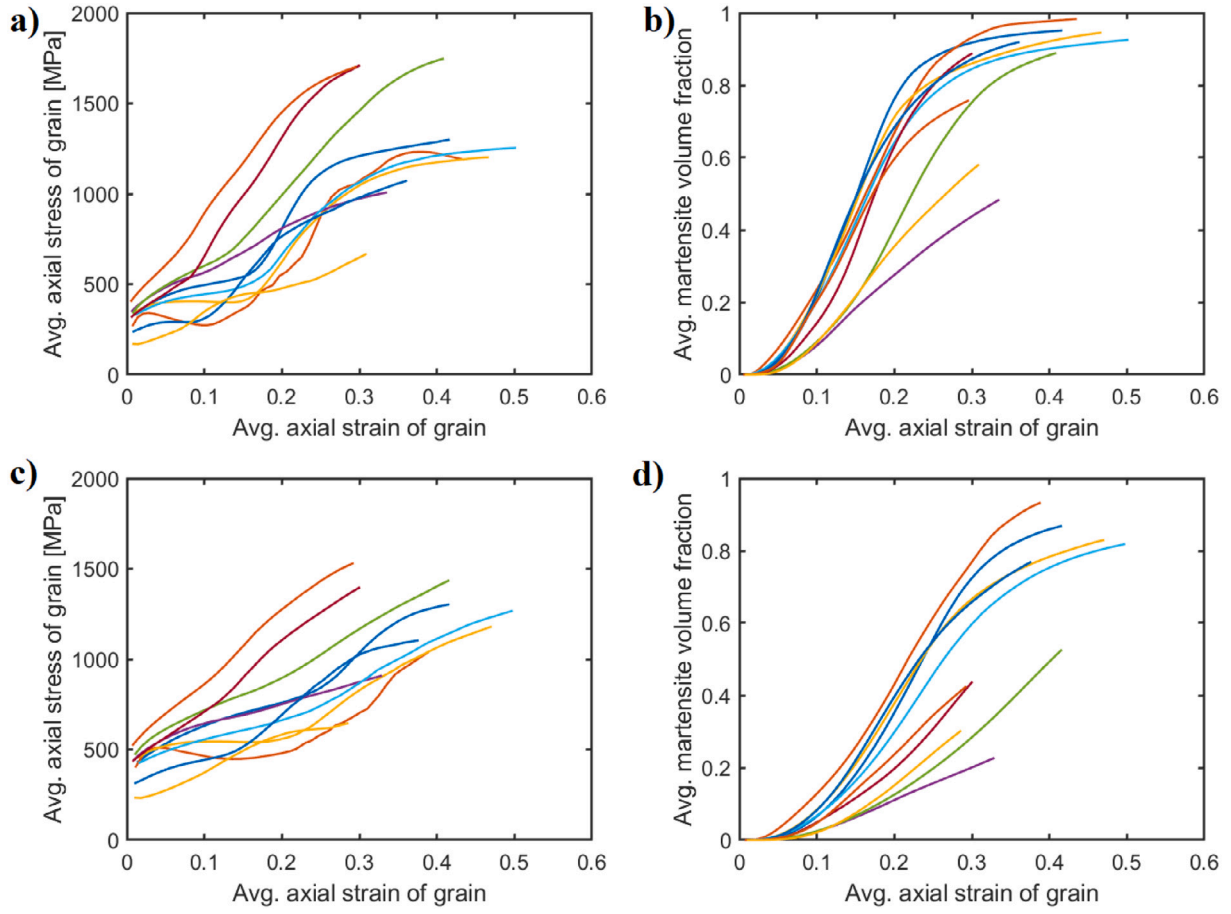


Fig. A.10. Stress-curves and martensite volume fraction of ten grains in the 3D aggregate, for strain rates (a), (c)  $2e^{-4}$  (b), (d)  $1.0 \text{ s}^{-1}$ . Macroscopic axial true strain is 33% at the end of simulation.

the changed transformation temperature value. In Fig. A.7d we assume twice as high latent heat for the simulations ( $\lambda_T^a = 40 \text{ kJ/kg}$ ).

The model response demonstrates that temperature has a significant influence on the phase transformation rate. The weakest effect is observed for the choice of  $\theta_T = 803 \text{ K}$  due to the large span of temperature range controlling the thermal contribution driving phase transformation. Decreased  $\theta_T$  values in Figs. A.7b, c lead to more pronounced variations as temperature increases. Phase transformation becomes almost fully suppressed when temperature is above  $300 \text{ C}$  and the small volume fractions predicted by the model are heavily mechanically induced. Decrease in strain hardening caused by dislocation slip as a function of increased temperature also explains the decreasing transformation rate, as low slip resistance attracts more plastic deformation by definition in the model. The results demonstrate the critical influence of thermally driven parametrization of the model, condensed to the approximation of transformation temperature  $\theta_T$  and latent heat  $\lambda_T^a$ . Another crucial aspect is the ratio between critical transformation stress  $f^{cr}$  and thermal contribution  $f^{th}$ . Keeping in mind that for the transformation to happen we need to satisfy constraint  $f^{th} > f^{cr} - f^m$ , where mechanical part  $f^m$  is a product of prevailing stress tensor.

The 301LN has very distinctive strain hardening capability that affects the magnitude of stress tensor when plastic flow is to occur. In a scenario that a material owns less strain hardening potential the thermal contribution is expected to gain more relevance when the mechanical stresses are generally lower. To address the sensitivity of latent heat and more pronounced thermal driving force, Fig. A.7d shows a set of curves with higher approximated latent heat  $\lambda_T^a = 40 \text{ kJ/kg}$  (versus  $20 \text{ kJ/kg}$ ). This choice increases the thermal driving force by double and thus the critical threshold is increased for transformation

accordingly to avoid a great flipover in the competition between slip and phase transformation. However, the ratio between mechanical contribution and thermal contribution is changed drastically so that thermal contribution is more dominant.

It is observed that the model becomes again more sensitive to temperature changes within  $120 \text{ K}$ , e.g., when comparing  $-40 \text{ C}$ ,  $24 \text{ C}$  and  $80 \text{ C}$ . In the light of temperature sensitivity analysis, we consider that the present model parametrization is suitable to a wide range of strain rates at room temperature. Model's prediction capability could be extended to a wider range of temperatures in another scope focusing on typical engineering operational temperatures, e.g., below zero for arctic use or high temperature applications. Also, the significance of the model formulation as is towards such engineering use cases is emphasized by these findings. Further experimental and modeling work, however, is then required to establish a well-posed predictive capability. More detailed thermal contribution constitutive formulation might be required in this case.

#### A.1. Analysis of 3D and EBSD based polycrystal aggregates

The deformation of three dimensional polycrystalline aggregate was investigated. Fig. A.8 shows the simulated stress-strain curves together with the evolution of martensite volume fraction for the 2D aggregate, used for model parametrization in previous section, and for 3D aggregate with 400 grains. The aggregate level homogenized results show very similar behavior between the two aggregate types and no adjustment to material parameters was therefore performed. Most distinctive 5%–10% difference occurs in the 2D case, when the orientation distribution is changed for the same microstructure from

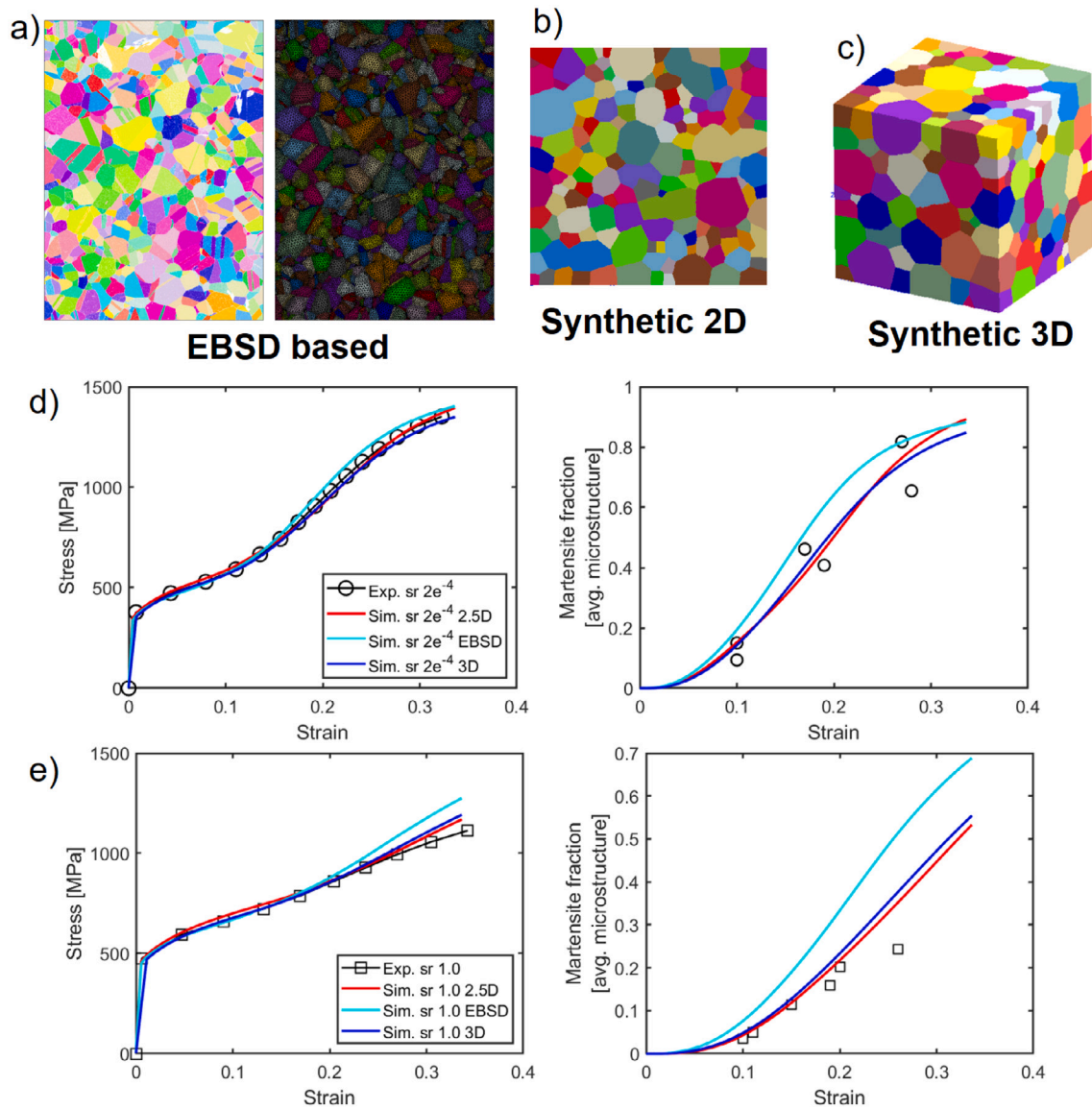


Fig. A.11. (a) EBSD based microstructure mesh, (b) synthetic 2D mesh, (c) synthetic 3D mesh, (d) and (e) stress-strain curves with martensite volume fractions for strain rates  $2 \cdot 10^{-4} \text{ s}^{-1}$  and  $1.0 \text{ s}^{-1}$ .

one random distribution to another. However, no effective difference exists between the used 2D and 3D aggregates.

Fig. A.9 illustrates equivalent stress and martensite volume fractions in the aggregate during a tensile test at three different macroscopic true strains. Stress heterogeneity increases with increasing volume fraction of martensite. Untransformed and partially transformed austenite grains act as relatively low stress regions. This again reflects that austenite phase is actively accommodating plastic deformation throughout the deformation history of the microstructure. To the same extent, Fig. A.10 shows that grains exhibiting strong phase transformation also carry out a significant part of the overall deformation. These grains exceed the straining of partially transformed grains in many occasions.

The characteristic excellent strain hardening capability of the material is based on the various grain level responses. The data for ten tracked grains (shown in Fig. A.10a,c) indicates that in initially hard grains (orientations) the flow stress increases from 2 up to almost 4 times of the initial yield stress. The same grains also face a high tendency to martensite transformation due to the elevated mechanical stress state driving transformation, which is expected to contribute notably to the strain hardening capability. Initially softer grains, as

indicated by their orientation with respect to tensile axis, undergo more modest strain hardening of  $1.2\text{--}2.0 \sigma_y$ . Strain softening may occur temporarily, which takes place after initiation of phase transformation as an additional deformation mechanism before hardening overtakes. This generates a small reduction in the macroscopic strain hardening rate of the material at around 5%–15% of strain, as seen in Fig. A.8a,c. As another future prospect, the initial dislocation structure in the transformed martensite remains open. High dislocation density in transformed untempered martensite, in particular, gains a role in the hardening behavior because it is expected to provide effective resistance for plastic deformation by dislocation slip. In the present modeling context, slip in martensite is introduced to generate the saturation behavior in flow stress in the grains at the end of the transformation process. This restricts the maximum average grain level stresses generally to below 2000 MPa.

Finally a third RVE strategy was investigated. An EBSD map was meshed and extruded to one element thickness. Hence, the following reviews three cases, (i) synthetic 2D microstructure with special 2.5D elements, (ii) synthetic 3D microstructure, (iii) extruded EBSD based microstructure. The EBSD based mesh uses wedge elements, the 2.5D case uses a triangular mesh and the full 3D tetra elements.



The boundary conditions were assigned to restrict lateral and vertical displacement of 2D (2.5D and EBSD) at the left and bottom edges of the domains, while top and right edges were bound with multi-point constraint to remain straight. For the EBSD based mesh, the displacement at the back and front side of the domain were bound ( $U_3 = 0$ ). The EBSD based mesh includes a realistic orientation distribution, annealing twins and in-plane grain morphology. However, it also lacks the in-depth grain interactions that is present in full 3D microstructure. Fig. A.11a–c shows the used microstructures.

The stress–strain response of the EBSD based mesh agrees well with the experimental curve at the lowest strain rate of  $2 \cdot 10^{-4} \text{ s}^{-1}$ . However, the volume fraction of martensite is overestimated in the simulations. Most significant difference in martensite fraction is observed at the higher  $1.0 \text{ s}^{-1}$  strain rate, where also the strain hardening rate is somewhat overestimated. Depending on the simulation strategy, the model parameters used in this work (e.g., critical transformation resistance  $f^{cr}$ ), may need further adjustment if EBSD based meshes are used. The EBSD based approach may be further utilized if in-situ tensile tests within SEM are performed with digital image correlation to have a direct comparison of the simulated and experimentally observed surface strains and evolution of local martensite content. This is, however, considered beyond the scope of this work. Instead, in the present work the parameters of Table 2, which result in similar predictions in the 2.5D and 3D cases, are used.

## References

- Alley, E., Neu, R., 2013. A hybrid crystal plasticity and phase transformation model for high carbon steel. *Comput. Mech.* 52, 237–255.
- Besson, J., Foerch, R., 1998. Object-oriented programming applied to the finite element method part I. general concepts. *Rev. Eur. Des Eléments Finis* 7 (5), 535–566.
- Choi, K., Liu, W., Sun, X., Khaleel, M., 2009. Microstructure-based constitutive modeling of TRIP steel: Prediction of ductility and failure modes under different loading conditions. *Acta Mater.* 57, 2592–2604.
- Delannay, L., Jacques, P., Pardoën, T., 2008. Modelling of the plastic flow of trip-aided multiphase steel based on an incremental mean-field approach. *Int. J. Solids Struct.* 45, 1825–1843.
- Devincere, B., Kubin, L., Hoc, T., 2006. Physical analyses of crystal plasticity by DD simulations. *Scr. Mater.* 54, 741–746.
- Fischer, F., Reisner, G., Werner, E., Tanaka, K., Cailletaud, G., Antretter, T., 2000. A new view on transformation induced plasticity (TRIP). *Int. J. Plast.* 16, 723–748.
- Fischlschweiger, M., Cailletaud, G., Antretter, T., 2012. A mean-field model for transformation induced plasticity including backstress effects for non-proportional loadings. *Int. J. Plast.* 37, 53–71.
- Hallberg, H., Håkansson, P., Ristinmaa, M., 2007. A constitutive model for the formulation of martensite in austenitic steels under large strain plasticity. *Int. J. Plast.* 23 (7), 1213–1239.
- Huang, J., X., Y., Gu, J., Chen, X., Xu, Z., 2012. Enhanced mechanical properties of type AISI301LN austenitic stainless steel through advanced thermo mechanical process. *Mater. Sci. Eng. A* 532, 190–195.
- Isakov, M., May, M., Hiermaier, S., Kuokkala, V.-T., 2016. A model for the strain rate dependent plasticity of a metastable austenitic stainless steel. *Mater. Des.* 106, 258–272.
- Järvenpää, A., Jaskari, M., Juuti, T., Karjalainen, P., 2017. Demonstrating the effect of precipitation on the mechanical stability of fine-grained austenite in reversion-treated 301LN stainless steel. *Metals* 7, 344.
- Järvenpää, A., Jaskari, M., Karjalainen, P., 2018. Reversed microstructures and tensile properties after various cold rolling reductions in AISI 301LN steel. *Metals* 8, 109.
- Järvenpää, A., Karjalainen, P., Jaskari, M., 2014. Effect of grain size on fatigue behavior of Type 301LN stainless steel. *Int. J. Fatigue* 65, 93–98.
- Kadkhodapour, J., Butz, A., Ziaei-Rad, S., Schmauder, S., 2011. A micro mechanical study on failure initiation of dual phase steels under tension using single crystal plasticity model. *Int. J. Plast.* 27, 1103–1125.
- Larour, P., Verleysen, P., Dahmen, K., Bleck, W., 2013. Strain rate sensitivity of pre-strained AISI 301LN2B metastable austenitic stainless steel. *Steel Res. Int.* 84 (1), 72–88.
- Lee, M.-G., Kim, S.-J., Han, H., 2010. Crystal plasticity finite element modeling of mechanically induced martensitic transformation (MIMT) in metastable austenite. *Int. J. Plast.* 26, 688–710.
- Lindroos, M., Laukkanen, A., Kuokkala, V.-T., 2017. A crystal plasticity approach for shear banding in hot rolled high-strength steels. *Metall. Mater. Trans. A* 48, 5608–5615.
- Liu, L., He, B., Huang, M., 2018. The role of transformation-induced plasticity in the development of advanced high strength steels. *Adv. Energy Mater.* 20, 1701083.
- Monnet, G., Mai, C., 2019. Prediction of irradiation hardening in austenitic stainless steels: Analytical and crystal plasticity studies. *J. Nuclear Mater.* 518, 316–325.
- Olson, G.B., Cohen, M., 1975. Kinetics of strain-induced martensitic nucleation. *Metall. Trans. A* 6A, 791–795.
- Otsuka, T., Brenner, R., Bacroix, B., 2018. FFT-based modelling of transformation plasticity in polycrystalline materials during diffusive phase transformation. *Int. J. Eng. Sci.* 127, 92–113.
- Papatriantafillou, I., Agoras, N., Haidemenopoulos, G., 2006. Constitutive modeling and finite element methods for TRIP steels. *Comput. Methods Appl. Mech. Engrg.* 195, 5094–5114.
- Park, T., Hector Jr., K., Hu, X., Abu-Farha, F., Fellingner, M., Kim, H., Esmailpour, R., Bourboghra, F., 2019. Crystal plasticity modeling of 3rd generation multi-phase AHSS with martensitic transformation. *Int. J. Plast.* 120, 1–46.
- Roters, F., Eisenlohr, P., Hantcherli, L., Tjahjanto, D., Bieler, T., Raabe, D., 2010. Overview of constitutive laws, kinematics, homogenization and multiscale methods in crystal plasticity finite-element modeling: Theory, experiments, applications. *Acta Mater.* 58, 1152–1211.
- Sohn, S., Song, H., Jo, M., Song, T., Kim, H., Lee, S., 2017. Novel 1.5 GPa-strength with 50%-ductility by transformation-induced plasticity of non-recrystallized austenite in duplex steels. *Nat. Sci. Rep.* 7 (1255), 1–9.
- Srivastava, A., Ghassemi-Armaki, H., Sung, H., Chen, P., Kumar, S., Bower, A., 2015. Micromechanics of plastic deformation and phase transformation in a three-phase TRIP-assisted advanced high strength steel: Experiments and modeling. *J. Mech. Phys. Solids* 78, 46–49.
- Sun, C., Guo, N., Fu, S., 2016. Modeling of slip, twinning and transformation induced plastic deformation for TWIP steel based on crystal plasticity. *Int. J. Plast.* 76, 186–212.
- Talonen, J., Nenonen, P., Pape, G., Hanninen, H., 2005. Effect of strain rate on strain-induced  $\gamma \rightarrow \alpha'$ -martensite transformation and mechanical properties of austenitic stainless steel. *Metall. Mater. Trans. A* 36, 421–432.
- Tjahjanto, D., Turteltaub, S., Suiker, A., 2006a. Crystallographically based model for transformation-induced plasticity in multiphase carbon steels. *Modell. Simul. Mater. Sci. Eng.* 14, 617–636.
- Tjahjanto, D., Turteltaub, S., Suiker, A., Van der Zwaag, S., 2006b. Transformation-induced plasticity in multiphase steels subjected to thermomechanical loading. *Modell. Simul. Mater. Sci. Eng.* 14, 617–636.
- Tjahjanto, D., Turteltaub, S., Suiker, A., Van der Zwaag, S., 2008. Modelling of the effects of grain orientation on transformation-induced plasticity in multiphase carbon steels. *Phil. Mag.* 88 (28–29), 3369–3387.
- Tomita, Y., Iwamoto, T., 1995. Constitutive modeling of TRIP steel and its application to the improvement of mechanical properties. *Int. J. Mech. Sci.* 37 (12), 1295–1305.
- Turteltaub, S., Suiker, A., 2005. Transformation-induced plasticity in ferrous alloys. *J. Mech. Phys. Solids* 53, 1747–1788.
- Turteltaub, S., Suiker, A., 2006a. Grain size effects in multiphase steels assisted by transformation-induced plasticity. *Int. J. Solids Struct.* 43, 7322–7336.
- Turteltaub, S., Suiker, A., 2006b. A multiscale thermomechanical model for cubic to tetragonal martensitic phase transformations. *Int. J. Solids Struct.* 43, 4509–4545.
- Vázquez-Fernández, N., Nyyssönen, T., Isakov, M., Hokka, M., Kuokkala, V.-T., 2019a. Uncoupling the effects of strain rate and adiabatic heating on strain induced martensitic phase transformations in a metastable austenitic steel. *Acta Mater.* 176, 134–144.
- Vázquez-Fernández, N., Soares, G., Smith, J., Seidt, J., Isakov, M., A., G., Kuokkala, V.-T., Hokka, M., 2019b. Adiabatic heating of austenitic stainless steels at different strain rates. *J. Dyn. Behav. Mater.* 5, 221–229.
- Wong, S., Madivala, M., Prah, U., Roters, F., Raabe, D., 2016. A crystal plasticity model for twinning- and transformation-induced plasticity. *Acta Mater.* 118, 140–151.
- Yadegari, S., Turteltaub, S., Suiker, A., 2012. Coupled thermomechanical analysis of transformation-induced plasticity in multiphase steels. *Mech. Mater.* 53, 1–14.
- Z-set package, 2013. Non-linear material & structure analysis suite. <https://www.zset-software.com>.
- Zaera, R., Rodríguez-Martínez, J., Rittel, D., 2013. On the Taylor-Quinney coefficient in dynamically phase transforming materials. *Int. J. Plast.* 40, 185–201.